

Role of 4-*tert*-Butylpyridine as a Hole Transport Layer Morphological Controller in Perovskite Solar Cells

Shen Wang,^{†,§} Mahsa Sina,^{†,§} Pritesh Parikh,[†] Taylor Uekert,[†] Brian Shahbazian,[†] Arun Devaraj,[‡] and Ying Shirley Meng^{*,†}

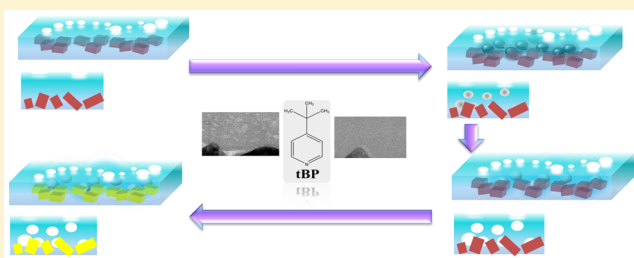
[†]Department of NanoEngineering, University of California, San Diego, 9500 Gilman Drive, La Jolla, California 92093, United States

[‡]Physical and Computational Sciences Directorate, Pacific Northwest National Laboratory, P.O. Box 999, Richland, Washington 99352, United States

S Supporting Information

ABSTRACT: Hybrid organic–inorganic materials for high-efficiency, low-cost photovoltaic devices have seen rapid progress since the introduction of lead based perovskites and solid-state hole transport layers. Although majority of the materials used for perovskite solar cells (PSC) are introduced from dye-sensitized solar cells (DSSCs), the presence of a perovskite capping layer as opposed to a single dye molecule (in DSSCs) changes the interactions between the various layers in perovskite solar cells. 4-*tert*-Butylpyridine (tBP), commonly used in PSCs, is assumed to function as a charge recombination inhibitor, similar to DSSCs. However, the presence of a perovskite capping layer calls for a re-evaluation of its function in PSCs. Using TEM (transmission electron microscopy), we first confirm the role of tBP as a HTL morphology controller in PSCs. Our observations suggest that tBP significantly improves the uniformity of the HTL and avoids accumulation of Li salt. We also study degradation pathways by using FTIR (Fourier transform infrared spectroscopy) and APT (atom probe tomography) to investigate and visualize in 3-dimensions the moisture content associated with the Li salt. Long-term effects, over 1000 h, due to evaporation of tBP have also been studied. Based on our findings, a PSC failure mechanism associated with the morphological change of the HTL is proposed. tBP, the morphology controller in HTL, plays a key role in this process, and thus this study highlights the need for additive materials with higher boiling points for consistent long-term performance of PSCs.

KEYWORDS: Perovskite solar cells, hole transport layer, transmission electron microscopy, focused ion beam, Fourier transform infrared spectroscopy, atom probe tomography



As an emerging photovoltaic technology with significant potential for commercialization, hybrid organic–inorganic perovskite solar cells (PSCs) have developed rapidly in recent years.^{1–4} With a certified 22.1% power conversion efficiency,⁵ compatibility with flexible substrates,^{6,7} and low fabrication energy consumption,^{8–10} PSCs are attracting enormous interest in both the academic and industrial field. As a p–i–n junction solar cell, a typical PSC has multiple layers and interfaces.^{11,12} Understanding the function of these components in PSCs can facilitate improvements in device efficiency and stability.¹³ Currently, a large number of researchers are focused on understanding the working mechanisms of the perovskite intrinsic layer and electron transport layer.^{11,14–16} However, investigations into the role of additives in the hole transport layer (HTL) remain relatively limited.^{17–19}

Traditionally, the HTL for PSCs consists of 2,2',7,7'-tetrakis(*N,N*-di-*p*-methoxyphenylamine)-9,9'-spirobifluorene (Spiro-OMeTAD), bis(trifluoromethane)sulfonimide lithium salt (LiTFSI), and 4-*tert*-butylpyridine (tBP) (For molecular structures of the HTL components see Supporting Information, Figure S1).² This combination was first applied in solid state dye-sensitized solar cells (ss-DSSC).^{20,21} In ss-DSSC, Spiro-

OMeTAD is the hole transport material, LiTFSI is the p-dopant, and tBP is the additive that acts as a recombination blocking agent.^{20,22} The function of tBP in ss-DSSC is the same as in liquid-based DSSC: tBP can adsorb on the surface of mesoporous TiO₂, which is the photoanode for DSSC. The adsorption of tBP on TiO₂: (1) suppresses direct contact between TiO₂ and electrolytes/hole transport materials to reduce charge recombination; and (2) negatively shifts the TiO₂ conduction band to increase the *V*_{oc} of DSSC.^{23,24} Due to the similarity in the device architecture for ss-DSSC and PSC, tBP is assumed to fulfill the same role in PSCs as in liquid-based DSSC or ss-DSSC.^{22,25,26}

However, in DSSC, dyes are discrete organic molecules which are difficult to organize into a continuous layer, whereas in PSCs, the intrinsic perovskite layer penetrates into the pores of the TiO₂ layer and also tops it as a capping layer. This suppresses the possibility of direct contact between tBP and

Received: May 29, 2016

Revised: August 14, 2016

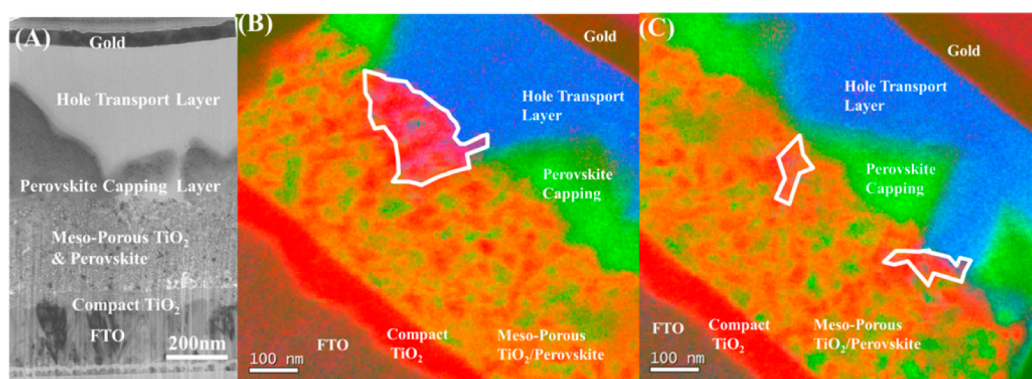


Figure 1. Correlation between perovskite coverage and HTL infiltration. (A) Bright-field TEM cross-section image of PSC prepared by focused ion beam (FIB). (B) Energy filtered-TEM mapping of a PSC cross-section with poor perovskite coverage. (Blue indicates Spiro-OMeTAD, red TiO_2 , and green perovskite. Regions where the HTL infiltrates the mesoporous TiO_2 are outlined in white.) (C) EF-TEM mapping of a PSC cross-section with rich perovskite coverage. (Blue indicates Spiro-OMeTAD, red TiO_2 , and green perovskite. Regions where the HTL infiltrates the mesoporous TiO_2 are outlined in white.)

TiO_2 . Moreover, in ss-DSSC, LiTFSI triggers the oxidation of Spiro-OMeTAD.^{27,28} In PSCs, despite the LiTFSI trigger, the oxidation reaction can only proceed if the perovskite layer also contributes to this process in a certain spectral range (>450 nm).²⁹ The combined effect of the perovskite capping layer and the spectral dependence of the oxidation reaction would allow new interactions among the components in HTL (specifically tBP) and between the HTL and intrinsic perovskite layer. This calls for a re-evaluation of the role of tBP as a charge recombination inhibitor and investigations into new interactions between the perovskite capping layer and tBP. Such detailed studies will ultimately help researchers clearly understand how PSCs work and provide effective solutions to the stability issue ensuring better success of this technology toward commercialization.

Recent reports have observed pin-holes in the HTL of PSCs.³⁰ These are considered to contribute to the poor stability of PSCs; oxygen and moisture in ambient environment can permeate through these pin-holes and cause degradation of the perovskite intrinsic layer, but the reason for the generation of pin-holes in HTL is still unclear.³¹

In this work, tBP is found to function as a morphology controller in the HTL of PSCs. Our observations suggest that, tBP reduces phase separation in the stock solution prior to spin-coating. This effect improves the film quality of the HTL by decreasing inhomogeneous regions. Using scanning electron microscopy (SEM), we prove that the presence of tBP significantly influences the HTL surface, by reducing the number of “pits” (also reported as pinholes^{30,31}). On the other hand, high-resolution cross-section transmission electron microscopy (TEM) images show that the HTL undergoes morphological changes after long-term (>1000 h) storage of PSC. With the help of atom probe tomography (APT), 3D visualization of the water distribution at HTL/perovskite interface is possible. By combining the phenomena we observe in TEM and APT, a PSC failure process mechanism is proposed, along with the morphological change of the HTL due to the evaporation of tBP. Our results indicate that tBP not only fulfills its function as previously reported for ss-DSSC but also acts as a morphology controller directly affecting device stability.

HTL Infiltration Behavior in PSCs. The majority of our samples in this study are prepared by focused ion beam (FIB) and were utilized high-quality SEM and TEM imaging:^{32–35}

The FIB milling/polishing process ensured that the sample had a smooth surface. Furthermore, using a FIB-based milling process allowed the sample to be thinned to the 100 nm required for TEM characterization. As shown in Figure 1A, the morphological contrast for every layer in PSC is distinguishable in BF-TEM. Based on FIB-prepared PSC samples for cross-section TEM imaging, we progress toward understanding the infiltration extent of HTL in PSCs. In ss-DSSC, the pore filling percentage of the HTL in a mesoporous TiO_2 photoanode is around 60–85% (the thickness of mesoporous TiO_2 is ~ 2.8 μm).^{36,37} These reports also demonstrate that reducing mesoporous TiO_2 layer thickness can increase the pore filling percentage. In mesoporous TiO_2 -based PSCs, the optimized thickness of mesoporous TiO_2 is around 300–400 nm.² If the HTL infiltrates into mesoporous TiO_2 to the same extent as it does in ss-DSSCs, the pore filling percentage in PSCs should be higher than 60–85% because of the thinner TiO_2 . However, our observations show that the pore filling percentage of the HTL in TiO_2 is much lower than 60% due to the presence of the perovskite layer that has infiltrated the mesoporous TiO_2 layer.

In PSC, the majority of the TiO_2 surface is covered with a perovskite capping layer, although some regions have poor coverage. Here, three components cross-section energy filtered TEM (EF-TEM) mapping is applied to display the infiltration behavior of HTL under the competing effect of the perovskite infiltration in mesoporous TiO_2 . Two PSC samples were prepared by FIB for EF-TEM, one with poor perovskite capping layer coverage on top of the mesoporous TiO_2 , the other one with rich perovskite capping layer coverage. As shown in Figure 1B, even in perovskite poor coverage regions, the infiltration of the HTL into mesoporous TiO_2 is limited. Most of the pores within the TiO_2 layer are filled with perovskite instead of HTL (Figure 1B green regions). In TiO_2 with pores deeper than 150 nm from the surface, no HTL is observed. However, when the perovskite coverage is better, as shown in Figure 1C, the area of TiO_2 infiltrated by the HTL is even smaller. The EF-TEM mapping indicated that under the competition of the perovskite, the infiltration of the HTL to mesoporous TiO_2 is limited. The more perovskite capping layer cover on top of TiO_2 the less the HTL can infiltrate into the mesoporous TiO_2 .

In previous reports, a penetration depth of ~ 100 nm for the HTL is observed, which show strong agreement with our

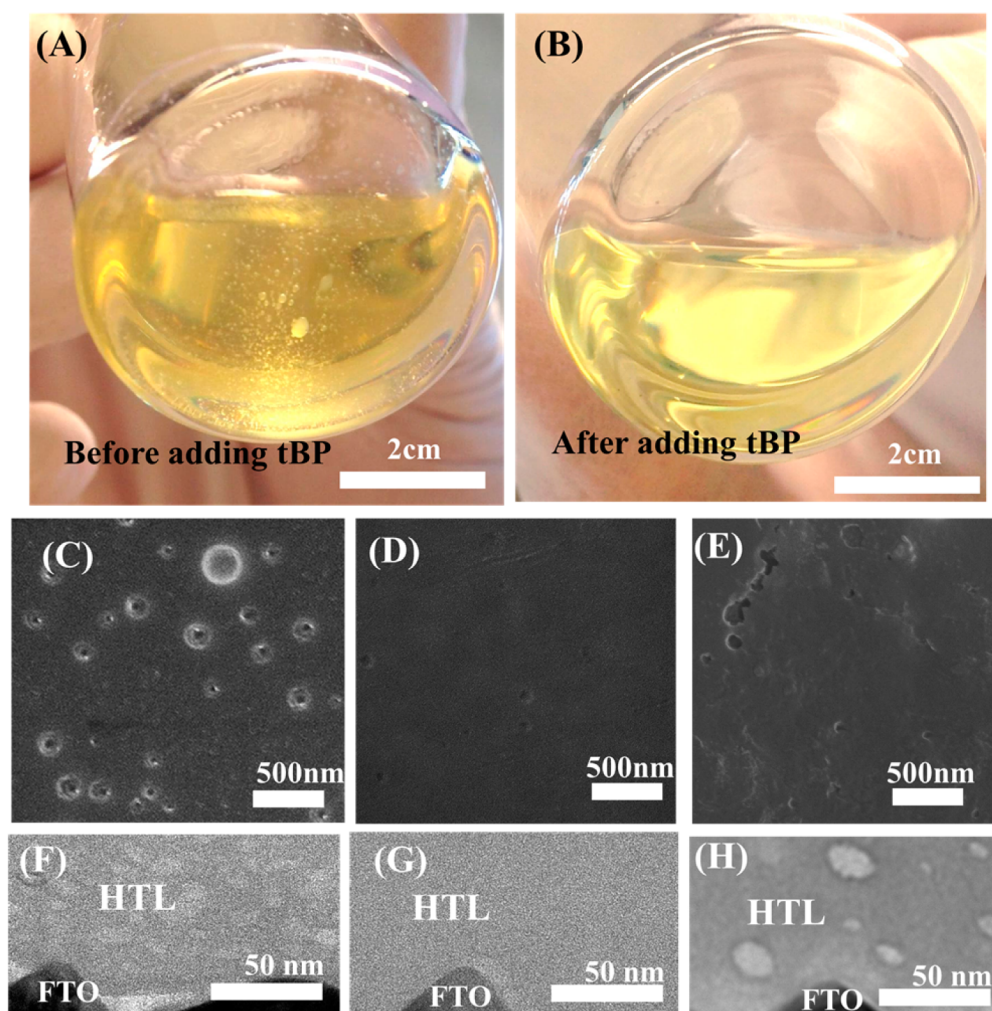


Figure 2. Photographs of HTL solution used for spin coating. (A) Before adding tBP and (B) after adding tBP. Top-view SEM images of the freshly prepared HTL (C) without tBP, (D) with tBP, and (E) with tBP after overnight vacuum treatment (10^{-4} Pa). Cross-section BF-TEM images of the freshly prepared HTL (F) without tBP, (G) with tBP, and (H) with tBP after overnight vacuum treatment (10^{-4} Pa).

experimental observations.³⁴ Since then, several groups have adopted superior fabrication procedures. A denser perovskite capping layer can further limit the pore-filling of the HTL in TiO_2 . Moreover, in planar heterojunction PSCs, which are devoid of mesoporous TiO_2 , the TiO_2 /HTL interface is further reduced. However, tBP is still used in majority of PSC architectures and device configurations. Hence, it should function differently in PSCs than in DSSCs.

tBP HTL Morphology Control Effect. Due to the limited penetration depth and low pore filling percentage, the TiO_2 /HTL interface in PSCs is much smaller than in ss-DSSCs. As a result, tBP acts only minimally to prevent direct contact between Spiro-OMeTAD and TiO_2 . However, as we observe, tBP does control the morphology of the HTL.

Before adding tBP, as shown in Figure 2A, the HTL solution used for spin-coating is phase-separated: the LiTFSI/acetonitrile solution (acetonitrile is the solvent to dissolve LiTFSI before adding to Spiro-OMeTAD solution) is immiscible with the Spiro-OMeTAD/chlorobenzene solution (chlorobenzene is the solvent for spin-coating of HTL). The majority of the LiTFSI/acetonitrile solution tends to accumulate at the bottom of the Spiro-OMeTAD/chlorobenzene solution as small liquid droplets. After adding tBP, as shown in Figure 2B, all liquid droplets disappear, which indicates that tBP improves the

solubility of LiTFSI in the Spiro-OMeTAD solution. It is possible that some complexes are formed by tBP and LiTFSI to reduce the phase separation in HTL solution and further influence the morphology of the HTL after spin-coating.

Because the existence of tBP guarantees the uniformity of HTL solution, as a result, it can affect the morphology of the spin-coated films. Several freshly prepared HTL samples were characterized by SEM/TEM as shown in Figure 2C–H. In Figure 2C, a top-view SEM image show that pits form on the surface of the HTL in the absence of tBP. After adding tBP, as Figure 2D displays, both the size and the number of the pits are significantly reduced. The homogeneous nature of the solution facilitates formation of a uniform film with a limited number of pits.

In order to prove that these pits in the HTL are indeed formed due to a lack of tBP, overnight vacuum treatment (10^{-4} Pa) was applied to a HTL with tBP. It is reported that tBP evaporates under vacuum environment and no X-ray photoelectron spectroscopy signals are observed related to tBP elements.³⁰ As shown in Figure 2E, the number and the size of the pits on the surface of the HTL increase after overnight vacuum treatment. The morphological change from Figure 2D to E can be attributed to the evaporation of tBP. Its disappearance/reduction causes the HTL film to revert back

to an inhomogeneous state, thereby resulting in the reappearance of more pits. Moreover, a few pits are located in the HTL even with tBP (Figure 2D), which we ascribe to the volatile nature of tBP on the surface. tBP can partially evaporate at the surface of the HTL, allowing a small portion of LiTFSI to regather and form pits.

To further study the morphological control of tBP on the HTL, FIB was used to prepare cross-section HTL samples with and without tBP. This enabled us to observe the morphology of the bulk of the film via BF-TEM at high resolution. Figure 2F–H are the BF-TEM images of the HTL cross-section without tBP, with tBP and with tBP after overnight treatment, respectively. In Figure 2F, without tBP, the HTL has an inhomogeneous morphology. Several bubble-like structures appear in the HTL. When the HTL contains tBP, as shown in Figure 2G, the bulk of the film is homogeneous. After overnight vacuum treatment of the tBP-contained film, Figure 2H, inhomogeneous regions appear again. For the various treatment histories, the morphology of the inhomogeneous regions in the tBP-free sample and that of the vacuum treatment tBP sample are slightly different, but the size and the distribution of the inhomogeneous regions for these two samples are in the same range.

In addition, we also characterized the tBP-contained film after thermal annealing. 200 °C was selected as the heat treatment temperature, as this temperature is above the boiling point of tBP and below the melting points for LiTFSI and Spiro-OMeTAD. The morphology of the top view (Supporting Information, Figure S2A) and the cross-section view (Supporting Information, Figure S2B) of the thermal annealing film is characterized. In Figure S2A, the number and size of the pits on the surface of the HTL increase after heat treatment. However, the morphology and location of the inhomogeneous regions in cross-section image of the annealed tBP sample is different compared with the vacuum treatment sample and the tBP-free sample. The inhomogeneous regions of the tBP-free and vacuum treatment samples show more small bubble-like regions that are mainly located at bulk of the film. These inhomogeneous regions show brighter contrast compared with the rest of the film. While in Figure S2B, the annealed sample's inhomogeneous regions are on top of the film, they show darker contrast compared with the rest of the film. These differences can be attributed to the melting of LiTFSI on 200 °C homogenizes bulk of the thermal annealing film; however, it still cannot prevent the surface morphological change due to the evaporation of tBP. In conjunction with the top view SEM and cross-section TEM results (Figure 2C–H, Supporting Information Figure S2A and B), it is obvious that tBP can affect both the surface and bulk morphology of HTL.

Previous reports described the nonuniform structure of the HTL as “pinholes”: the authors proposed that the pinholes pass through the entire HTL layer, which put moisture and air in direct contact with the surface of perovskite layer and trigger further degradation.^{30,31} If pinholes did indeed exist in the HTL, a cross-section TEM image of a PSC would reveal this specific morphology. However, the cross-section TEM images (Figures 1 and 2) prove that the HTL is uniform (in the presence of tBP). In Supporting Information, Figure S3, a cross-section BF-TEM image of a PSC showing a larger region for the HTL also indicates that the bulk of the HTL is homogeneous and contains no pinholes. On the other hand, the metal (top electrode)/HTL interface is not flat, which suggests that the surface morphology has shallow pits instead of

pinholes (Supporting Information, Figure S4). To demonstrate the difference between a “pit” and “pinhole” in the HTL, a picture is shown in Supporting Information, Figure S5: although the morphology of the HTL looks similar from a top view, in the cross-section the “pinholes” and “pits” are easy to distinguish. To get the accurate morphological information on HTL and to prevent the FIB process from damaging the sample, two measures were taken into our experiment: (1) Before FIB process, all samples were predeposited with a metal protecting layer (Pt or Ir 200 nm and then 2 μ m Pt), which can prevent the beam from damaging the top of the HTL. (2) During FIB thinning process, only 5 kV voltage and 7 pA current were applied to the sample when the sample thickness is smaller than 200 nm. This measure can minimize the beam-induced damage to only 10 nm.³⁸

HTL Morphological Change in PSCs. Apart from our observation of pits on the surface of the HTL (in the absence of tBP), its effect on the stability still needed further investigation. Since the evaporation of tBP can also lead to morphological change of the HTL as mentioned earlier, we suspect this effect exists in a real device and finally influences the device performance. To study this mechanism, we observe the long-term morphological change of the HTL in an unsealed full PSC. We store the PSC samples under ambient dark conditions with 10% moisture for 1000 h. Four samples for BF-TEM were prepared by FIB on the same cell after different storage times (0, 200, 500, and 1000 h).

As shown in Figure 1A, at the start, the HTL is homogeneous. As discussed before, that is because tBP promotes miscibility of LiTFSI and Spiro-OMeTAD. After 200 h, as Figure 3A displays, inhomogeneous dark regions appear on the HTL. These regions are due to the accumulation of Li salt which occurs due to the loss of tBP by evaporation. Figure 3B shows the morphology of the HTL after 500 h. The majority of the dark regions disappear, even as bubble-like structures are generated. This likely occurs because of the hygroscopicity of LiTFSI: moisture can easily react with the accumulated LiTFSI seen in Figure 3A. The hydration of LiTFSI therefore leads to the bubble structures in the HTL. Finally, in Figure 3C, after 1000 h, the perovskite has decomposed. These images display that the morphological change, in other words, the failure process of PSCs, is initiated from the HTL instead of the perovskite layer followed by eventual degradation of perovskite. The related photo current density–voltage curves (*J*–*V* curves) and device parameters for the stored cells are shown in Figure 3D and Table 1. Compare with the freshly prepared PSCs (12.6%), the performance decays of the 250 h (10.9%) and 500 h (7.51%) PSCs are not as obvious as the 1000 h PSCs. It is consistent with the TEM results since the decomposition of the perovskite layer at the first 500 h is limited while at 1000 h, perovskite layer has decomposed.

On the basis of the morphology control effect of tBP on HTL and the failure process of the PSCs, a mechanism regarding the long-term morphological change in a perovskite solar cell is presented now. As displayed in Figure 4, at the start (right after device fabrication), the existence of tBP guarantees a uniform HTL, with minimal shallow pits located on the surface the of the HTL. After tBP evaporates, the Li salt accumulates, shown as dark circular regions. These regions are further hydrated to create void structures in the HTL which finally lead to decomposition of the perovskite layer. It should be noted that these events may not strictly proceed one after

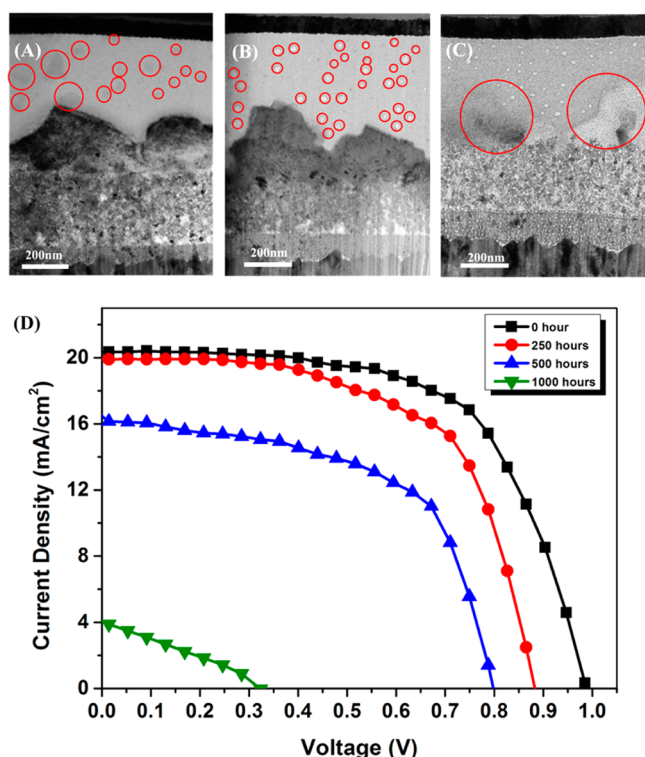


Figure 3. BF-TEM cross-section images of the long-term morphological change in the HTL after (A) 200 h storage (inhomogeneous regions in the HTL marked with red circles), (B) 500 h storage (bubble structures in the HTL marked with red circles), and (C) 1000 h storage (degraded perovskite capping layer marked by red circles). (D) J - V curves of the stored perovskite solar cells. Each curve is the average of 10 cells prepared at the same batch of the TEM sample.

Table 1. Cell Parameters of the Perovskite Solar Cells Stored for 1000 h at 10% Humidity Ambient Dark Conditions

	V_{OC} (V)	J_{SC} (mA/cm ²)	fill factor	efficiency (%)
0 h	0.987	20.38	0.63	12.6
250 h	0.886	19.97	0.62	10.9
500 h	0.799	16.16	0.58	7.51
1000 h	0.331	3.90	0.29	0.38

the other but may instead occur at the same time. During the LiTFSI hydration process, for instance, the decomposition of the perovskite may have already begun since water is already in the HTL.

Humidity Accumulation Characterizations in PSCs. To further confirm that the lack of tBP can lead to the increasing amount of water in HTL, four fresh-prepared Spiro-OMeTAD films with various components combinations were characterized by Fourier transform infrared spectroscopy (FTIR). As shown in Figure 5, films of pure Spiro-OMeTAD (black line), Spiro-OMeTAD/tBP (red line), and Spiro-OMeTAD/tBP/LiTFSI (dark green line) all display similar peaks. That is because the primary component of the HTL film is Spiro-OMeTAD (in accordance with the weight percentage of the HTL spin-coating solution). However, a water peak is observed in the Spiro-OMeTAD/LiTFSI sample (blue line). This broad peak at ~ 3600 cm⁻¹ corresponds to the O–H stretching mode of water in FTIR. In contrast, no water peak appears in the Spiro-OMeTAD/tBP/LiTFSI sample (dark green line). This indicates that tBP prevents the accumulation of LiTFSI in

Spiro-OMeTAD films, thereby reducing the possibility of LiTFSI hydration since the material is well dispersed throughout the Spiro-OMeTAD and shielded by tBP. The mechanism of how tBP prevents LiTFSI hydration at a chemical level will be the scope of our future work.

The FTIR study confirmed the presence of moisture in films without tBP, but in order to visualize that moisture truly exists in the HTL for a full cell device structure, we utilized laser-assisted atom probe tomography (APT). With the unique ability of APT to obtain three-dimensional (3D) position information and compositional mapping of energy materials,^{39,40} we constructed a map of the water accumulated in PSCs at the HTL/perovskite interface. The PSC devices were stored for over 500 h prior to sample preparation for APT analysis. This corresponds to the morphology of Figure 3B. In this state, as mentioned before, tBP would evaporate allowing the accumulation of LiTFSI and its possible hydration.

Figure 6A displays a perovskite solar cell cross section wedge lifted out for preparing an atom probe needle specimen. Various layers in the device architecture are clearly visible. The annular milling process during final stages of the needle specimen preparation was controlled to retain the HTL layer on the specimen apex and then proceed to the perovskite layer below, with the interface in between. In Figure 6B, the APT maps show the clear boundary between F (red) and Pb (blue), corresponding to the perovskite/HTL interface. Pb and F maps are used since they are the sole indicators for perovskite and LiTFSI respectively, not present in any other layers. Although fluorine signatures can be obtained from the FTO (fluorine doped tin oxide) layer, atomic positions of F above the Pb region do not conform to the position of the FTO layer. Another caveat is the low analysis temperature used for APT analysis (60 K) which is below the phase transition temperature for the intrinsic perovskite layer. We do not expect that the phase transition would affect the ordering of the layers and the interfaces.

As shown in Figure 6C, the chemical map for water indicates a strong concentration at the specimen apex region as opposed to the entire region of analysis. To the best of our knowledge, such a strong concentration could not possibly occur from a background signal (see Supporting Information, Figure S6 for a more quantitative analysis). This region of water accumulation is concurrent with regions of high F concentration. Thus, we conclude that water accumulates in the HTL rather than the perovskite layer.

In comparison to similar chemical maps for F and H₂O, using freshly prepared samples (see Supporting Information, Figure S7 for more details) with no aging, the total counts for H₂O and F ions are 5 times higher. These observations are also consistent with our TEM results and FT-IR data. In PSCs samples stored in ambient under dark conditions, the amount of tBP in the HTL is reduced due to its relatively low boiling point and volatile nature. As a result, the HTL prefers to adsorb water due to the hygroscopicity of LiTFSI.

In conclusion, the function of tBP in PSCs was re-evaluated to understand its influence on device stability. Due to the limited penetration depth of HTL into mesoporous TiO₂, it is unlikely that the additive serves only to prevent contact between the Spiro-OMeTAD and TiO₂ layers as traditionally assumed. Based on our observations, tBP functions as a morphological controller for the HTL. It prevents phase separation of LiTFSI and Spiro-OMeTAD during spin-coating of the solution, resulting in a uniform HTL film. The absence of

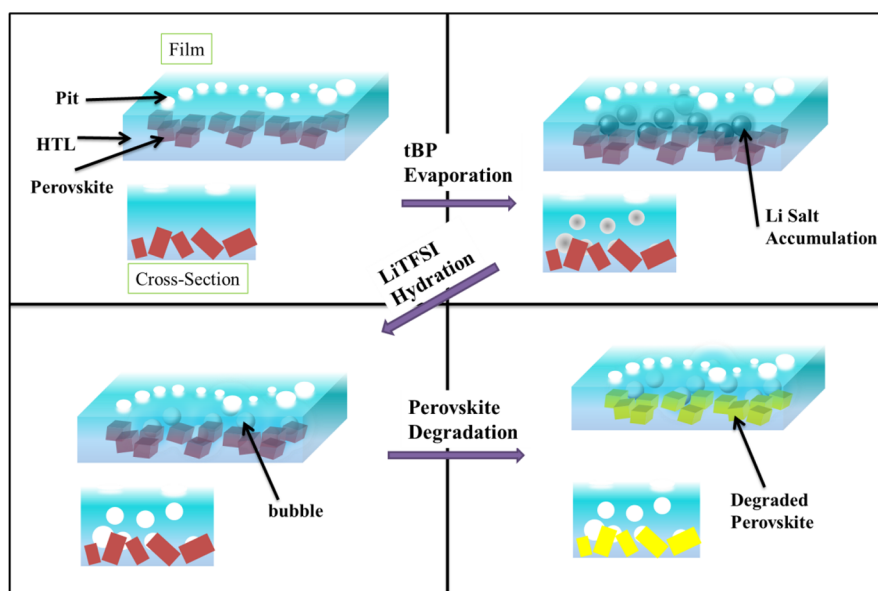


Figure 4. Schematic of the morphological change of the HTL/perovskite layers as they are stored in dark conditions.

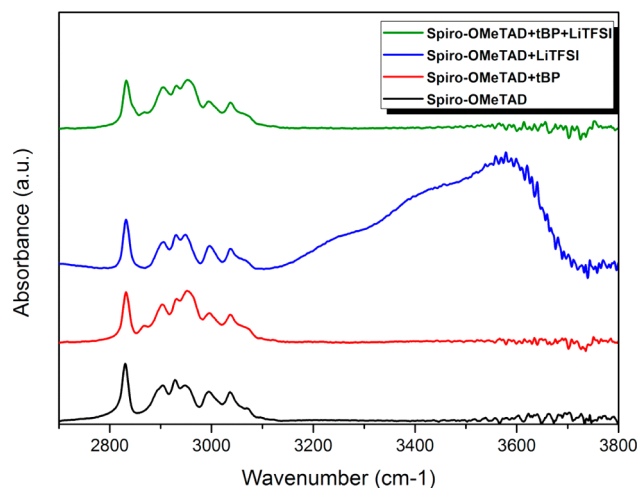


Figure 5. FTIR spectra of Spiro-OMeTAD films with various component combinations.

tBP leads to inhomogeneous films and also causes the appearance of large pits on the surface of the HTL. tBP-free HTL easily absorbs water due to the hygroscopicity of accumulated LiTFSI and further lowers the stability of PSCs.

In PSCs stored in ambient dark conditions for 1000 h, the slow evaporation of tBP (as it is the only liquid component in PSCs) leads to all of the above-discussed phenomena. Li salt accumulates and generates “dark regions” in the HTL. These dark regions then turn into void bubble structures due to the hydration of Li salt. Finally, the water contained in the HTL contributes to perovskite degradation. Since the evaporation of tBP is a primary contributor to the poor stability of PSCs, we suggest that the performance of PSCs can be enhanced by utilizing other pyridine derivatives that can fulfill the same functions as tBP but have much higher boiling points.

■ ASSOCIATED CONTENT

§ Supporting Information

The Supporting Information is available free of charge on the [ACS Publications website](https://doi.org/10.1021/acs.nanolett.6b02158) at DOI: 10.1021/acs.nanolett.6b02158.

Experimental methods for this research, molecular structures of the components in the HTL for PSCs, and more detailed FIB-TEM and APT information (Figures S1–S7) ([PDF](#))

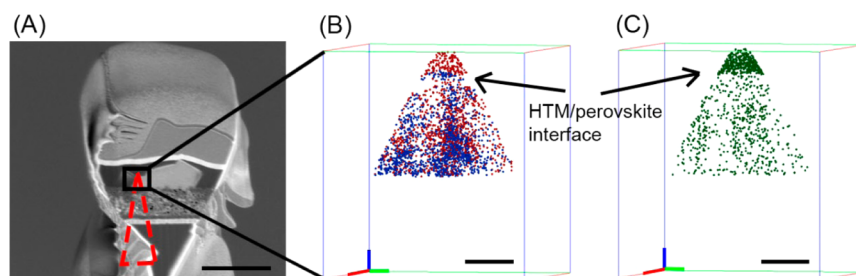


Figure 6. 3D APT maps of HTL/perovskite layers after long-term storage (>500 h). (A) SEM image of an APT sample section attached on a Si micropost prior to annular milling by FIB. The red section shows the analysis area. (The scale bar is 1 μm .) (B) 3D elemental maps of Pb (blue dots, from perovskite $\text{CH}_3\text{NH}_3\text{PbI}_3$) and F (red dots, from TFSI[−] in HTL). (C) APT map of H_2O showing its distribution in 3D. (Scale bars in B and C are 10 nm. Shown in green is the x -axis, red corresponds to the y -axis, and blue is the z -axis.)

AUTHOR INFORMATION

Corresponding Author

*E-mail (Y.S.M.): shirleymeng@ucsd.edu.

Author Contributions

§(S.W., M.S.) These authors contributed equally.

Notes

The authors declare no competing financial interest.

ACKNOWLEDGMENTS

This work is supported by the seed funding from Sustainable Power and Energy Center (SPEC) under Frontier of Innovation Award by Vice Chancellor of Research at University of California San Diego. S. Wang gratefully acknowledges the Jacobs Graduate Fellowship by Jacobs School of Engineering at UC San Diego. P. Parikh acknowledges financial support from the Qualcomm Mentor Fellowship. This work was performed in part at the San Diego Nanotechnology Infrastructure (SDNI), a member of the National Nanotechnology Coordinated Infrastructure, which is supported by the National Science Foundation (Grant ECCS-1542148). The EF-TEM images were performed with an approval of the National Center for Electron Microscopy at Lawrence Berkeley National Laboratory. Sample preparation and analysis for atom probe tomography was performed using EMSL, a DOE National User Facility sponsored by the Office of Biological and Environmental Research and located at Pacific Northwest National Laboratory.

REFERENCES

- (1) Liu, M.; Johnston, M. B.; Snaith, H. J. *Nature* **2013**, *501*, 395–398.
- (2) Burschka, J.; Pellet, N.; Moon, S.-J.; Humphry-Baker, R.; Gao, P.; Nazeeruddin, M. K.; Grätzel, M. *Nature* **2013**, *499*, 316–320.
- (3) Yang, W. S.; Noh, J. H.; Jeon, N. J.; Kim, Y. C.; Ryu, S.; Seo, J.; Seok, S., II. *Science* **2015**, *348*, 1234–1237.
- (4) Kojima, A.; Teshima, K.; Shirai, Y.; Miyasaka, T. *J. Am. Chem. Soc.* **2009**, *131*, 6050–6051.
- (5) NREL Efficiency Chart. http://www.nrel.gov/ncpv/images/efficiency_chart.jpg (accessed Aug 1, 2016).
- (6) Kaltenbrunner, M.; Adam, G.; Glowacki, E. D.; Drack, M.; Schwödiauer, R.; Leonat, L.; Apaydin, D. H.; Groiss, H.; Scharber, M. C.; White, M. S.; Sariciftci, N. S.; Bauer, S. *Nat. Mater.* **2015**, *14*, 1032–1039.
- (7) Yin, X.; Chen, P.; Que, M.; Xing, Y.; Que, W.; Niu, C.; Shao, J. *ACS Nano* **2016**, *10*, 3630–3636.
- (8) Li, R.; Xiang, X.; Tong, X.; Zou, J.; Li, Q. *Adv. Mater.* **2015**, *27*, 3831–3835.
- (9) Ball, J. M.; Lee, M. M.; Hey, A.; Snaith, H. J. *Energy Environ. Sci.* **2013**, *6*, 1739.
- (10) Fu, F.; Feurer, T.; Jäger, T.; Avancini, E.; Bissig, B.; Yoon, S.; Buecheler, S.; Tiwari, A. N. *Nat. Commun.* **2015**, *6*, 8932.
- (11) Edri, E.; Kirmayer, S.; Henning, A.; Mukhopadhyay, S.; Gartsman, K.; Rosenwaks, Y.; Hodes, G.; Cahen, D. *Nano Lett.* **2014**, *14*, 1000–1004.
- (12) Marchioro, A.; Teuscher, J.; Friedrich, D.; Kunst, M.; van de Krol, R.; Moehl, T.; Grätzel, M.; Moser, J.-E. *Nat. Photonics* **2014**, *8*, 250–255.
- (13) Nguyen, W. H.; Bailie, C. D.; Unger, E. L.; McGehee, M. D. *J. Am. Chem. Soc.* **2014**, *136*, 10996–11001.
- (14) Xiao, Z.; Yuan, Y.; Shao, Y.; Wang, Q.; Dong, Q.; Bi, C.; Sharma, P.; Gruverman, A.; Huang, J. *Nat. Mater.* **2014**, *14*, 1–18.
- (15) Xu, X.; Chen, Q.; Hong, Z.; Zhou, H.; Liu, Z.; Chang, W. H.; Sun, P.; Chen, H.; Marco, N.; Wang, M.; Yang, Y. *Nano Lett.* **2015**, *15*, 6514–6520.
- (16) Kim, H. S.; Lee, J. W.; Yantara, N.; Boix, P. P.; Kulkarni, S. A.; Mhaisalkar, S.; Grätzel, M.; Park, N. G. *Nano Lett.* **2013**, *13*, 2412–2417.
- (17) Choi, H.; Mai, C.-K.; Kim, H.-B.; Jeong, J.; Song, S.; Bazan, G. C.; Kim, J. Y.; Heeger, A. J. *Nat. Commun.* **2015**, *6*, 7348.
- (18) Liu, Y.; Chen, Q.; Duan, H.-S.; Zhou, H.; Yang, Y.; Chen, H.; Luo, S.; Song, T.-B.; Dou, L.; Hong, Z.; Yang, Y. *J. Mater. Chem. A* **2015**, *3*, 11940–11947.
- (19) You, J.; Meng, L.; Song, T.-B.; Guo, T.-F.; Yang, Y.; Chang, W.-H.; Hong, Z.; Chen, H.; Zhou, H.; Chen, Q.; Liu, Y.; De Marco, N.; Yang, Y. *Nat. Nanotechnol.* **2015**, *11*, 75–81.
- (20) Krüger, J.; Plass, R.; Cevey, L.; Piccirelli, M.; Grätzel, M.; Bach, U. *Appl. Phys. Lett.* **2001**, *79*, 2085–2087.
- (21) Yuan, W.; Zhao, H.; Hu, H.; Wang, S.; Baker, G. L. *ACS Appl. Mater. Interfaces* **2013**, *5*, 4155–4161.
- (22) Dualeh, A.; Moehl, T.; Tétreault, N.; Teuscher, J.; Gao, P.; Nazeeruddin, M. K.; Grätzel, M. *ACS Nano* **2014**, *8*, 362–373.
- (23) Boschloo, G.; Häggman, L.; Hagfeldt, A. *J. Phys. Chem. B* **2006**, *110*, 13144–13150.
- (24) Haque, S. A.; Palomares, E.; Cho, B. M.; Green, A. N. M.; Hirata, N.; Klug, D. R.; Durrant, J. R. *J. Am. Chem. Soc.* **2005**, *127*, 3456–3462.
- (25) Park, N. G. *J. Phys. Chem. Lett.* **2013**, *4*, 2423–2429.
- (26) Li, W.; Dong, H.; Wang, L.; Li, N.; Guo, X.; Li, J.; Qiu, Y. *J. Mater. Chem. A* **2014**, *2*, 13587–13592.
- (27) Cappel, U. B.; Daeneke, T.; Bach, U. *Nano Lett.* **2012**, *12*, 4925–4931.
- (28) Abate, A.; Leijtens, T.; Pathak, S.; Teuscher, J.; Avolio, R.; Errico, M. E.; Kirkpatrick, J.; Ball, J. M.; Docampo, P.; McPherson, I.; Snaith, H. J. *Phys. Chem. Chem. Phys.* **2013**, *15*, 2572–2579.
- (29) Wang, S.; Yuan, W.; Meng, Y. S. *ACS Appl. Mater. Interfaces* **2015**, *7*, 24791–24798.
- (30) Hawash, Z.; Ono, L. K.; Raga, S. R.; Lee, M. V.; Qi, Y. *Chem. Mater.* **2015**, *27*, 562–569.
- (31) Jung, M.-C.; Raga, S. R.; Ono, L. K.; Qi, Y. *Sci. Rep.* **2015**, *5*, 9863.
- (32) Divitini, G.; Cacovich, S.; Matteocci, F.; Cinà, L.; Di Carlo, A.; Ducati, C. *Nat. Energy* **2016**, *1*, 15012.
- (33) Bergmann, V. W.; Weber, S. A. L.; Javier Ramos, F.; Nazeeruddin, M. K.; Grätzel, M.; Li, D.; Domanski, A. L.; Lieberwirth, I.; Ahmad, S.; Berger, R. *Nat. Commun.* **2014**, *5*, 5001.
- (34) Nanova, D.; Kast, A. K.; Pfannmöller, M.; Müller, C.; Veith, L.; Wacker, I.; Agari, M.; Hermes, W.; Erk, P.; Kowalsky, W.; Schröder, R. R.; Lovrinčić, R. *Nano Lett.* **2014**, *14*, 2735–2740.
- (35) Zhou, Y.; Vasiliev, A. L.; Wu, W.; Yang, M.; Pang, S.; Zhu, K.; Padture, N. P. *J. Phys. Chem. Lett.* **2015**, *6*, 2292–2297.
- (36) Docampo, P.; Hey, A.; Guldin, S.; Gunning, R.; Steiner, U.; Snaith, H. J. *Adv. Funct. Mater.* **2012**, *22*, 5010–5019.
- (37) Snaith, H. J.; Humphry-Baker, R.; Chen, P.; Cesar, I.; Zakeeruddin, S. M.; Grätzel, M. *Nanotechnology* **2008**, *19*, 424003.
- (38) Kim, S.; Jeong Park, M.; Balsara, N. P.; Liu, G.; Minor, A. M. *Ultramicroscopy* **2011**, *111*, 191–199.
- (39) Devaraj, A.; Gu, M.; Colby, R.; Yan, P.; Wang, C. M.; Zheng, J. M.; Xiao, J.; Genc, A.; Zhang, J. G.; Belharouak, I.; Wang, D.; Amine, K.; Thevuthasan, S. *Nat. Commun.* **2015**, *6*, 8014.
- (40) Santhanagopalan, D.; Schreiber, D. K.; Perea, D. E.; Martens, R. L.; Janssen, Y.; Khalifah, P.; Meng, Y. S. *Ultramicroscopy* **2015**, *148*, 57–66.